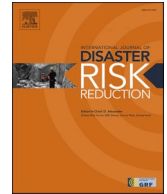




ELSEVIER

Contents lists available at [ScienceDirect](https://www.sciencedirect.com)

International Journal of Disaster Risk Reduction

journal homepage: www.elsevier.com/locate/ijdr

Disaster resilience analysis framework for lifeline networks: Integrating reliability, redundancy, and recoverability

Taeyong Kim^a, Sang-ri Yi^b, Ji Hyeon Kim^{c,*}, Ji-Eun Byun^{d,**}

^a Department of Civil Systems Engineering, Ajou University, Suwon, Republic of Korea

^b Department of Civil and Environmental Engineering, University of California Berkeley, Berkeley, USA

^c Advanced Railroad Civil Engineering Division, Korea Railroad Research Institute, Uiwang, Republic of Korea

^d James Watt School of Engineering, University of Glasgow, Scotland, UK

ARTICLE INFO

Keywords:

Disaster resilience
Lifeline networks
System reliability
Resilience triangle
Power network
Transportation network

ABSTRACT

Resilience analysis aims to quantify the risk of a system and evaluate its ability to recover from a damaged state and restore functionality to its original condition. This study presents a framework for assessing the disaster resilience of lifeline networks, emphasizing both hazard resistance and post-hazard recovery capabilities. To quantitatively assess resilience performance, the framework introduces indices for three key criteria: reliability, redundancy, and recoverability. The reliability index reflects the structural performance of network components, the redundancy index captures the system-level functional capacity, and the recoverability index evaluates the ability to restore network functionality following disruption. The resilience triangle concept is used to define the redundancy and recoverability indices. Estimating these indices for various initial disruption scenarios enables the identification of the most vulnerable situations that influence the resilience of the system, thus aiding in the development of effective pre-hazard mitigation strategies. Additionally, scenario-specific performance curves, representing the recovery process through the redundancy and recoverability indices, support rapid and informed decision-making in the aftermath of a hazard. The proposed framework is demonstrated through case studies of electricity and transportation networks. This research contributes to improving the safety and functionality of critical infrastructure systems in the face of diverse disasters.

1. Introduction

Lifeline networks—such as utility distribution, transportation, and communication—are essential for enabling socioeconomic activities and sustaining the livelihoods of urban populations. As populations grow and societal demands evolve, the importance of lifeline networks continues to increase. Consequently, ensuring the uninterrupted functioning of lifeline networks during both natural and human-induced disasters is crucial. According to Koks et al. [1], the global expected annual loss from seismic damage to road and railway networks is approximately 1.2 billion US dollars. In addition, in 2019, coordinated attacks on the oil facilities in Saudi Arabia disrupted nearly half of the nation's oil production, which at the time accounted for approximately 5% of the global daily oil supply [2].

* Corresponding author.

** Corresponding author.

E-mail addresses: jhkim06@krrri.re.kr (J.H. Kim), ji-Eun.Byun@glasgow.ac.uk (J.-E. Byun).

<https://doi.org/10.1016/j.ijdr.2025.105436>

Received 8 January 2025; Received in revised form 20 March 2025; Accepted 28 March 2025

Available online 29 March 2025

2212-4209/© 2025 The Authors. Published by Elsevier Ltd. This is an open access article under the CC BY license (<http://creativecommons.org/licenses/by/4.0/>).

Modern disaster management frameworks increasingly adopt proactive resilience strategies to mitigate the impact of extreme hazards and manage unprecedented consequences [3–7]. Kilanitis and Sextos [4] explored expected losses in road systems by considering the states of key network components through a probabilistic framework. Li et al. [6] incorporated both time-independent and time-varying hazard interarrival models to quantify the long-term resilience of highway bridges under various natural hazards. Wang et al. [7] proposed a three-stage model to quantify and analyze the resilience of power networks, focusing on different repair strategies.

Despite the extensive exploration of disaster resilience performance in lifeline networks, two main limitations emerge. First, most studies rely on a single measure or index, either at the component- or system-level, to assess network performance, providing limited information for effective intervention decisions [8]. Lifeline networks are complex systems comprising multiple interdependent structural and nonstructural components, requiring both component-level and system-level performance measures for a more comprehensive evaluation.

A notable exception is Kwon and Song [5], who assessed network performance using multiple indices, but their system-level performance measure focuses primarily on network topology—i.e., the connectivity between source and end nodes—rather than functionality or consequence. The functionality or consequence is essential because lifeline networks provide critical services to entire communities. Disruptions to their components can have wide-ranging consequences. Further details of this framework are presented in Section 2.2.

Second, most of the existing research primarily focuses on assessing system performance during the recovery phase following a hazard rather than jointly considering the potential risks and vulnerabilities before the event. This research employs the resilience triangle model developed by Bruneau et al. [3]. It has proven useful in optimizing recovery processes across various lifeline networks, including railway systems [9], road transportation networks [10], power grids [11], transportation networks [12], pipelines [13], and water distribution systems [14]. However, given the critical role of lifeline networks in urban areas, it is vital to make effective decisions for post-hazard recovery and ensure system safety and functionality before a hazard strikes.

To address these gaps, this study proposes a holistic and probabilistic framework for assessing the disaster resilience performance of lifeline networks. The novelty of the proposed methodology can be summarized in two key aspects. First, we introduce new mathematical definitions for three key resilience indices—reliability, redundancy, and recoverability—which are systematically evaluated across a range of potential initial disruption scenarios. The reliability index quantifies the structural performance of network components, while the redundancy index captures the system-level functional capacity of the network. The recoverability index assesses the ability of society to efficiently restore network functionality following a disruption. Note that previous research on system-reliability-based disaster resilience analysis [5,15] has primarily considered redundancy as a means of preventing cascading failures. Contrastingly, the present study considers overall performance degradation owing to hazard impacts, offering a more comprehensive perspective. Moreover, previous frameworks lack a detailed methodology to evaluate recoverability, which is a critical component of resilience analysis and a key factor distinguishing our proposed approach from conventional risk analysis frameworks. Second, the resilience triangle [3] is employed to define the redundancy and recoverability indices, integrating both pre-hazard damage prevention efforts and post-hazard recovery strategies. These indices are calculated for each disruption scenario, enabling the identification of the most vulnerable failure paths in terms of resilience and the formulation of proactive mitigation plans. Furthermore, the recovery process, represented by the resilience triangle for each disruption scenario, facilitates rapid and effective decision-making in the aftermath of a hazard. Incorporating grid asset vulnerability into the resilience triangle method significantly advances previous resilience triangle model frameworks [3,9–14,16–18]. Additionally, integrating the recovery process enhances system-reliability-based disaster resilience analysis frameworks [5,15], providing a more comprehensive assessment of resilience.

The proposed framework is demonstrated through numerical case studies of power and transportation networks. For the power network, an electricity system with 9 substations is analyzed, while for the transportation network, a larger-scale system comprising 76 unidirectional edges and 24 nodes is examined to illustrate the practical applicability of the proposed method.

The remainder of this paper is organized as follows. Section 2 reviews two conventional resilience assessment frameworks: (1) the resilience triangle model and (2) the system-reliability-based disaster resilience analysis method. In Section 3, the two frameworks are integrated to introduce a novel resilience assessment approach. The framework combines both pre-hazard resilience performance evaluation and post-hazard optimal decision-making tools. In Section 4, the effectiveness of the proposed framework is demonstrated through two numerical case studies. Finally, Section 5 summarizes the findings, conclusions, and potential future research directions.

2. Review of resilience analysis frameworks

According to ASME Innovative Technologies Institute [19], resilience is defined as the comprehensive ability of a system to resist both external and internal disruptions while maintaining its original functionality and rapidly and fully restoring functionality following a failure. Various frameworks have been developed to quantify the disaster resilience performance of infrastructure systems [3,5,15]. While each framework possesses distinct characteristics and advantages, no single approach fully captures all the desirable properties outlined in [15]. The framework proposed by Bruneau et al. [3] is particularly effective in characterizing system performance during the recovery phase, while the framework developed by Kwon and Song [5] emphasizes grid asset vulnerability. Inspired by their complementary strengths, we develop a unified methodology that addresses both post-disaster recovery dynamics and grid asset vulnerability. Therefore, in this section, we review resilience performance assessment frameworks proposed by Bruneau et al. [3] and Kwon and Song [5].

2.1. Resilience triangle model

The resilience triangle model, introduced by Bruneau et al. [3], incorporates four resilience criteria—robustness, redundancy, resourcefulness, and rapidity—to evaluate the disaster resilience performance of civil structural systems. Robustness refers to the ability of a system to withstand disastrous events without experiencing significant damage, redundancy accounts for the presence of alternative components that can maintain functionality even if some parts are damaged, resourcefulness refers to the ability to effectively manage and best utilize available resources for recovery, and rapidity represents the speed of restoring full functionality after a disaster. The resilience triangle model (Fig. 1) visually illustrates the loss of functionality caused by a disaster and the subsequent recovery process over time. The model provides a framework to quantify resilience characteristics by representing the area under the curve as a measure of the performance loss and recovery of the system.

Extensive research has been conducted to define and apply the resilience triangle model for lifeline networks under various hazard scenarios [20–23]. Efforts have also focused on determining optimal recovery sequences to minimize the area of the resilience triangle [24–26]. While the framework effectively monitors system performance during recovery and aids in developing optimal recovery strategies, it does not fully capture the inherent ability of the system to prevent functional loss prior to a disaster.

2.2. System-reliability-based disaster resilience analysis frameworks for lifeline networks

Lim et al. [15] characterized the resilience of civil structural systems using three criteria: reliability, redundancy, and recoverability. Reliability is defined as the ability to prevent initial disruptions in network components. Redundancy refers to the ability to avert progressive failures and degradation of network performance. Finally, recoverability refers to the capacity of engineers and society to implement effective strategies to quickly restore the functionality of a network following a disruption. Compared to the framework presented in Section 2.1, the concept of reliability in the study by Lim et al. [15] aligns with the notion of robustness described by Bruneau et al. [3]. The concept of redundancy is equivalent in both frameworks, while recoverability in the framework introduced by Lim et al. [15] encompasses both resourcefulness and rapidity.

Building on the definitions provided by Lim et al. [15], Kwon and Song [5] proposed reliability (β) and redundancy (π) indices for network systems. These indices are evaluated for each initial disruption scenario. The initial disruption scenarios are defined as a collection of the components' states within a lifeline network, considered binary (failure or survival), while the performance of the system is determined by the connectivity between key components. The indices are mathematically defined as follows:

$$\beta_i = -\Phi^{-1}(P(F_i|H)) = -\Phi^{-1}(P(\cap_{e \in S_i} E_e|H)) \tag{1}$$

$$\pi_i = -\Phi^{-1}(P(F_{sys}|F_i, H)) = -\Phi^{-1}\left(\frac{P(\cup_l (\mathcal{E}_l \cap_{e \in S_i} E_e)|H)}{\Phi(-\beta_i)}\right) \tag{2}$$

where $\Phi^{-1}(\cdot)$ represents the inverse cumulative distribution function of the standard normal distribution; $P(F_i|H)$ represents the probability of occurrence of the i -th initial disruption scenario F_i given the hazard H ; E_e represents the failure event of component e in the network; S_i is a set of failed components associated with F_i ; $P(F_{sys}|F_i, H)$ describes the probability of system level failure given F_i and H ; and \mathcal{E}_l denotes the l -th cut set event.

The resilience performance of the lifeline network is then assessed using the following resilience threshold concept [15,27].

$$\Phi(-\pi_i)\Phi(-\beta_i) < P_{dm} / (\lambda_H N_F) \tag{3}$$

and a reliability–redundancy (β – π) diagram illustrated in Fig. 2, where λ_H denotes the annual mean occurrence rate of H ; and N_F indicates the number of initial disruption scenarios. Following the concept of *de minimis* risk [28], the recommended scale of P_{dm} is in the order of $10^{-7}/yr$ for civil structural systems.

While this framework provides valuable insights into the complex interplay between component-level and system-level capacity in resisting hazard loads, it has several limitations. First, although the resilience threshold in Eq. (3) is based on the assumption that initial disruption scenarios are mutually exclusive and collectively exhaustive (MECE) [15,27], the formulations in Eqs. (1) and (2) use non-exclusive initial scenario sets, which can lead to an underestimation of reliability and redundancy performance. Second, while

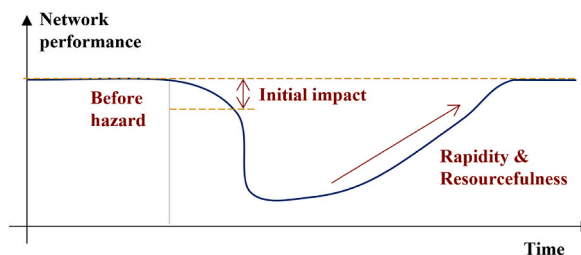


Fig. 1. Resilience triangle model.

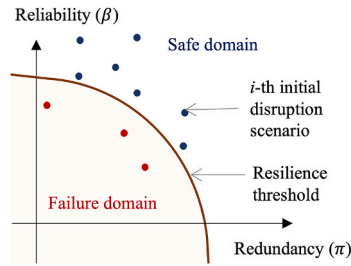


Fig. 2. Reliability–redundancy (β – π) diagram.

incorporating progressive (or cascading) failures initiated by the selected disruption scenario into the redundancy indices is considered ideal, Eq. (2) does not account for this aspect. Third, assessing network performance based solely on the connectivity between key nodes is insufficient because lifeline networks are typically designed to provide essential services to entire communities. Therefore, integrating more comprehensive system functionality and performance measures is necessary to accurately quantify redundancy. Fourth, the formulations do not address the uncertainties associated with structural responses under stochastic excitations. Finally, the framework lacks a recoverability index, which is a critical criterion to evaluate the resilience performance of lifeline networks.

Section 3 introduces a new resilience analysis framework for lifeline networks that addresses the gaps in both existing frameworks. This new framework enables the development of pre-hazard disaster mitigation strategies and supports optimal post-hazard decision-making for effective response and rapid recovery.

3. Resilience analysis framework for lifeline networks

3.1. Underlying assumptions for defining resilience indices

We adopt the three criteria from the system-reliability-based disaster resilience analysis framework to characterize the resilience performance of lifeline networks. To facilitate a clearer understanding of the indices introduced in this section, we first present a hypothetical infrastructure network comprising five nodes, as illustrated in Fig. 3. Note that the illustration provides a seamless linkage between the mathematical formulations and their interpretations in the context of network resilience performance; it does not serve as a test case for implementing the framework or assessing the resilience performance of the hypothetical network. The components within the lifeline network can assume binary states (failure or survival), in line with the assumptions of the previous framework in Section 2.2. In this example, with the nodes selected as components for the resilience analysis, a total of $2^5 = 32$ initial disruption scenarios are generated. Although the examples considered in this paper focus solely on node failures within the network, the framework can also accommodate scenarios involving the simultaneous failure of both nodes and edges.

Consider progressive failure following the initial failure of a few nodes, analogous to load redistribution in structures such as buildings and cable-stayed bridges. In the case of a power network, this may be caused by overcurrent, undervoltage, or abnormalities in generators. For transportation networks, progressive failure can result from congestion, which leads to the dysfunction of road components. Owing to uncertainties in potential progressive failure paths, the i -th initial disruption scenario F_i may lead to different final damage states $G_j, j = 1, \dots, N_G$, where N_G indicates the total number of possible damage states.

For simplification in the hypothetical network example, we assume that the set of final damage states $\{G_j, j = 1, \dots, N_G\}$ is identical to the initial disruption scenario set $\{F_i, i = 1, \dots, N_F\}$. For instance, in the hypothetical lifeline network, the initial failure scenario of $\{E_1\bar{E}_2\bar{E}_3E_4E_5\}$ (survival of components 1, 4, 5 and failure of components 2, 3) could result in one of the following final damage states: $\{E_1\bar{E}_2\bar{E}_3E_4E_5\}, \{E_1E_2\bar{E}_3E_4E_5\}, \{E_1\bar{E}_2E_3E_4E_5\}$, and $\{E_1E_2E_3E_4E_5\}$, where \bar{E}_e represents the survival event of component e in the network. However, in some lifeline networks, certain components may not be directly affected by natural hazards but may fail because of the interdependencies within the network, or in some cases, certain initial disruption scenarios may not be observed in the final damage states. In such cases, these components are not included in the initial disruption scenarios but are incorporated into the final damage states. Thus, in such instances, the set of final damage states $\{G_j, j = 1, \dots, N_G\}$ is not identical to the initial disruption scenario set $\{F_i,$

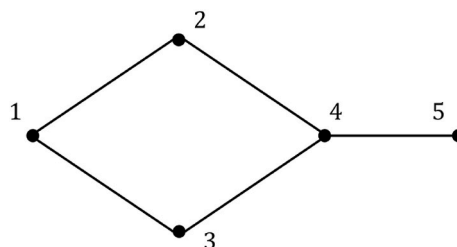


Fig. 3. Hypothetical lifeline network where numbers 1, 2, 3, 4, and 5 indicate the five nodes of the network.

$i = 1, \dots, N_F\}$.

A recovery process for each damage state is determined using the resilience triangle model. In particular, the performance of the network during recovery is defined by the estimated sequence of node recoveries and the available resources. The resilience triangle model is applied to each final damage state. Fig. 4 illustrates an example configuration of the resilience triangle (or trapezoid) model for one of the final damage states. In Fig. 4, P_{NS} represents the performance of the network before the occurrence of a hazard, i.e., the normal state of network performance.

The initial performance loss, recovery time, and shape of the recovery curve vary across different damage states. Notably, various functional performance measures can be used to define the system-level performance of the lifeline network (i.e., the y-axis in the resilience triangle model in Fig. 4). These measures could include factors such as the loss of load in a power network or the transport capacity of a railway network, based on the application context and various socioeconomic factors. The detailed simulation methods used to estimate recovery and performance are referenced in numerous previous studies [9–14,25,29–32], and this work demonstrates how such methods can be integrated into the proposed resilience assessment framework. Moreover, the proposed framework can be further extended to incorporate different perspectives, including an economic perspective, and probabilistically consider various uncertainties by integrating existing research efforts, such as those proposed by Broccardo et al. [16].

Note that the resilience triangle model, as depicted in Fig. 4, assumes that a disruption results in a decrease in the performance measure. However, in certain cases—travel time in a transportation network—the performance function may increase post-disruption. In such scenarios, resilience measures should be interpreted in terms of the “area below the curve” rather than the “area above the curve,” as conventionally defined. Alternatively, the reciprocal of the selected performance measure can be used to define the y-axis of the resilience triangle model, ensuring consistency in interpretation.

3.2. Reliability, redundancy, and recoverability indices

The reliability index is first defined as follows, representing the structural capacity of network components to avoid initial disruptions:

$$\beta_i = -\Phi^{-1}(P(F_i|H)) = -\Phi^{-1}\left(\int P(F_i|im, H)f_{im}(im|H)dim\right) \tag{4}$$

where im represents an intensity measure (IM) of hazards H ; $P(F_i|im, H)$ represents the occurrence probability of the i -th initial disruption scenario given im and is referred to as a reliability curve; and $f_{im}(im|H)$ represents the probability density function (PDF) of im given H . Note that in this study, “IM” refers to the intensity measure and not the importance measure, which is a widely used acronym in the field of reliability engineering. To ensure that the initial disruption scenarios form a MECE set, the i -th initial disruption scenario F_i is defined as

$$F_i = (\cap_{e \in S_i} E_e) \cap (\cap_{e \in S_i^c} \bar{E}_e) \tag{5}$$

in which S_i^c is the complement of set S_i . Compared to Eq. (1), where the initial disruption scenarios are structured as a MECE set, a more precise evaluation of resilience performance—whether the system is resilient or not—can be achieved. Furthermore, the ability of the index to account for aleatoric uncertainty in hazards allows for an effective assessment of system resilience under stochastic excitations. The details of the resilience performance assessment are discussed in Section 3.3. The definition in Eq. (4) is exactly equivalent to the individual structure-scale reliability index discussed by Yi and Kim [27], with the only difference being in the definition of F_i .

The redundancy index for the i -th initial disruption scenario, π_i is newly defined in terms of the expected system performance loss PL_i as follows:

$$\pi_i = f_\pi(PL_i) = f_\pi\left(\sum_j pl_{ij} \cdot P(G_j|F_i)\right) \tag{6}$$

where $f_\pi(\cdot)$ represents the redundancy indexing function, pl_{ij} denotes the system performance loss for the j -th damage state G_j owing to i -th initial disruption scenario, and $P(G_j|F_i)$ represents the probability that the initial disruption scenario F_i results in the final damage state G_j . The maximum degradation of system performance for the j -th damage state (i.e., “performance loss” as shown in Fig. 4) is

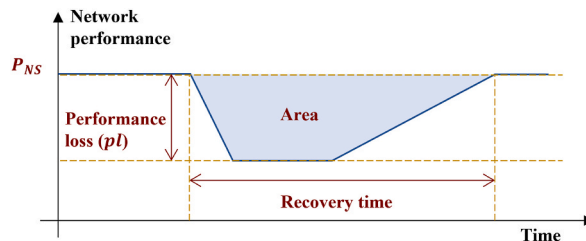


Fig. 4. Resilience triangle model for each final damage state.

employed for pl_{ij} . Eq. (2) is a special case of Eq. (6), where the performance loss is defined as $P(F_{sys}|G_j)$ where F_{sys} indicates the connectivity status of the system, and the redundancy indexing function is chosen to be $-\Phi^{-1}(\cdot)$.

As a more redundant system experiences less performance loss after a hazard event, PL_i and π_i should be inversely proportional to each other. A possible redundancy indexing function can be defined based on the level of degradation in system performance relative to normal operation, expressed as:

$$f_{\pi}(PL_i) = \frac{P_{NS} - PL_i}{P_{NS}} \tag{7}$$

where P_{NS} represents the system performance under normal operation, which remains constant across the damage states. The function is designed to map PL_i to a value between zero and one. Moreover, if no progressive failure occurs, only one damage state (i.e., $G_j = F_i$) exists. Thus, Eq. (6) simplifies to

$$\pi_i = f_{\pi}(PL_i) \tag{8}$$

The recoverability index for the i -th initial disruption scenario, γ_i is defined in terms of the expected nominal recovery time T_i given scenario F_i as follows:

$$\gamma_i = f_{\gamma}(T_i) = f_{\gamma}\left(\sum_j \frac{a_{ij}}{pl_{ij}} \cdot P(G_j|F_i)\right) \tag{9}$$

where $f_{\gamma}(\cdot)$ represents the recoverability indexing function; and a_{ij} represents the area above the system performance curve during the recovery of j -th damage state due to i -th initial failure scenario, which is illustrated as the ‘‘Area’’ in Fig. 4. One possible choice is to use a linear recoverability indexing function

$$f_{\gamma}(T_i) = \max(k_R T_i + 1, \gamma_{min}) \tag{10}$$

where $k_R \leq 0$ is a slope parameter that controls the inherent tendencies of stakeholders regarding the consideration of recoverability levels in resilience analysis, and $\gamma_{min} > 0$ indicates the lower bound of the index. Similar to the redundancy indexing function, the recoverability indexing function is designed to convert T_i to a value between zero and one. Moreover, as in Eq. (8), if no progressive failure occurs, Eq. (9) simplifies to

$$\gamma_i = f_{\gamma}\left(\frac{a_i}{PL_i}\right) \tag{11}$$

Although we adopted Eqs. (7) and (9) for the redundancy and recoverability indexing functions, respectively, in the numerical examples, alternative mapping functions between physical quantities and resilience indices can be employed when more detailed information is available.

3.3. Resilience assessment

Risk refers to the potential for an undesirable outcome, typically characterized as a function of two primary variables: (1) the probability of an event occurring and (2) the magnitude of impact or loss if the event occurs. Mathematically, risk is quantified by multiplying the probability of occurrence by the corresponding amount of loss and summing these values over all possible events. Similarly, we define the resilience gap under hazard H as the annually aggregated amount of expected cumulative functionality loss, using the following mathematical definition:

$$\text{Resilience Gap} = \sum_{i=1}^{N_F} P(F_i|H) \cdot A_i \cdot \lambda_H = \sum_{i=1}^{N_F} P(F_i|H) \cdot PL_i \cdot T_i \cdot \lambda_H \tag{12}$$

in which λ_H denotes the annual mean occurrence rate of the hazard H ; and A_i refers to the expected area above the system performance curve during the recovery process for the i -th initial disruption scenario, which is given by

$$A_i = \sum_j a_{ij} \cdot P(G_j|F_i) \tag{13}$$

Compared to the conventional definition of risk, two key differences are noted. First, A_i is employed to define the resilience gap, accounting for both the scale of impact and the duration of recovery. To illustrate the importance of introducing the ‘‘Area’’ concept, which considers both system performance loss PL and recovery time T , consider the following examples:

- Widespread but short-duration event: A 1-h power outage affecting an entire urban area may have relatively minor consequences for most residents, with minimal disruption to daily activities, such as refrigeration. However, even a short power interruption can be critical for essential facilities, such as hospitals and semiconductor fabrication plants, which require an uninterrupted power supply for their operations.

- **Localized but long-duration event:** By contrast, a two-day power outage affecting a small portion of the urban area could have severe consequences for the affected population, which may include significant food spoilage, disruption of essential services, and potential health risks.

Second, the resilience gap of the system is determined by summing the functionality losses across all initial disruption scenarios. In particular, we decompose the resilience gap across a set of initial disruption scenarios to gain a clearer understanding of the impacts resulting from different failure paths. For example, if the recoverability of region “A” is superior to that of region “B,” decision-makers can consider implementing preventive measures for grid assets in region “B,” as greater efforts and resources are expected to reduce the consequences after a disaster.

By representing $P(F_i|H)$, PL_i , and T_i through the reliability, redundancy, and recoverability resilience indices in Eqs. (4), (6) and (9), respectively, and introducing an upper threshold for the resilience gap denoted as RG^* , Eq. (12) can be rewritten as

$$\sum_{i=1}^{N_F} \Phi(-\beta_i) \cdot f_{\pi}^{-1}(\pi_i) \cdot f_{\gamma}^{-1}(\gamma_i) \cdot \lambda_H \leq RG^* \tag{14}$$

Assuming each initial disruption scenario contributes equally to the total resilience gap, a threshold can be assigned for each scenario as follows:

$$\Phi(-\beta_i) \cdot f_{\pi}^{-1}(\pi_i) \cdot f_{\gamma}^{-1}(\gamma_i) \leq \frac{RG^*}{\lambda_H N_F} \tag{15}$$

where $RG^*/\lambda_H N_F$ represents the resilience threshold for each initial disruption scenario.

RG^* is determined by stakeholders or organizations, and its value may vary depending on their tolerance toward functionality loss—considering both the internal characteristics of the network system and its influence on other infrastructural networks (gas, transportation, power, and water) and the broader community [33–35]. Owing to these variations, RG^* should be considered a subjective measure that reflects the priorities and resilience tolerance of decision-makers. To enhance the robustness and applicability of the proposed approach, future work should focus on developing methodologies to better quantify and standardize the resilience threshold value, accounting for these different perspectives. One possible approach, similar to risk analysis frameworks, is to create a structured process in which decision-makers utilize a matrix representation, with rows corresponding to probability values and columns representing performance loss levels. Colors, typically ranging from green to red, can be incorporated into the table to visually represent the severity of resilience associated with each slot. This framework would enable stakeholders to categorize different disruption scenarios based on their resilience objectives. Furthermore, sensitivity analyses could be performed to assess how variations in RG^* influence resilience assessment outcomes, providing critical insights into the robustness of the system under different resilience thresholds.

Using Eq. (15), the resilience threshold can be illustrated graphically. Fig. 5 presents a β - π - γ diagram, where the resilience threshold is depicted as a gray surface and the resilience indices for each initial disruption scenario are represented as dots. Similar to the β - π diagram in Fig. 2, if an index fails to meet the resilience requirement of Eq. (14), the corresponding dot is colored red; conversely, dots are colored blue when they satisfy the requirement. As depicted in the figure, for certain initial disruption scenarios, a high value in one of the indices (e.g., a high-reliability index, indicating a low probability of occurrence for the disruption scenario) can make the scenario satisfy the resilience requirement, even if the other two indices have lower values (e.g., low redundancy and recoverability).

Based on the diagram and Eq. (15), several strategies can be considered to implement preventive interventions that enhance the

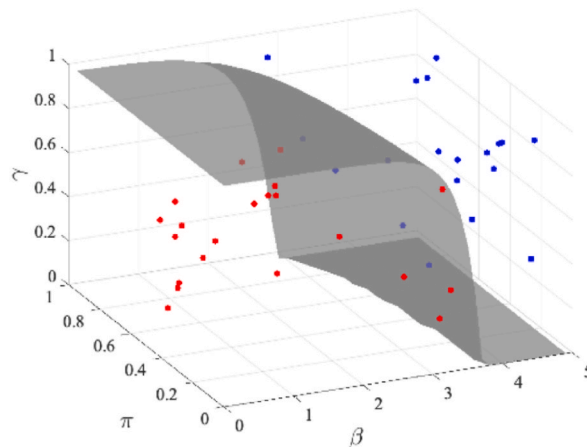


Fig. 5. β - π - γ diagram for lifeline network.

resilience performance of lifeline networks. First, improving the reliability index requires reducing the failure probability of each component in the network; a possible approach to achieve this is retrofitting network assets. Second, additional redundant components (e.g., providing alternative transportation routes) should be installed to enhance the redundancy index, ensuring that system performance remains stable even if multiple components fail. Third, improving the recoverability index involves preparing adequate recovery resources and determining an optimal recovery sequence to minimize the area under the system performance curve. Moreover, considering budget constraints and the trade-offs between improving each index, the framework helps decision-makers prioritize infrastructure upgrades and resilience-enhancing measures effectively.

The quantification of reliability, redundancy, and recoverability indices, alongside the graphical tool illustrated in Fig. 5, enables a comprehensive assessment of the resilience performance of lifeline networks. The quantification is essential to develop strategies to mitigate the impacts of hazards before their occurrence. The most vulnerable components within the network can be identified by analyzing the distance of initial disruption scenarios from the resilience limit-state. This information enables decision-makers to prioritize the installation of monitoring sensors on these critical components, ensuring real-time performance tracking during hazard events. Moreover, this framework facilitates the development of optimal retrofit strategies. By leveraging optimization algorithms, such as reinforcement learning, the framework can help shift initial disruption scenarios that fail to meet resilience thresholds into a safer domain while optimizing budget allocation, thereby enhancing overall system resilience. Furthermore, as the redundancy and recoverability indices define the performance curve of the system during the recovery process, the proposed framework supports rapid post-hazard decision-making. It provides a catalog of pre-computed consequences for various disruption scenarios, enabling stakeholders to utilize the predetermined recovery sequence and the recovery curve shown in Fig. 4 to accelerate their response to catastrophic events and recover quickly to original functionality.

4. Numerical investigations

4.1. Power grid network

To illustrate the proposed resilience analysis framework, the IEEE 9-bus system is introduced as a case study [36]. The IEEE 9-bus system comprises nine buses (or substations), three generators, three loads, and nine transmission lines, as shown in Fig. 6. The generators are connected to Buses 1, 2, and 3, while the loads are distributed across Buses 5, 6, and 8. The system is designed to represent a small section of a larger power grid. Detailed data for the generators, loads, and transmission lines are provided in Appendix A. Notably, the load values in the original IEEE 9-bus model have been scaled by a factor of 2.4 to analyze load shedding. Further information on the IEEE 9-bus system is provided in [37].

This study evaluates the resilience of the IEEE 9-bus system under seismic hazards by using a fragility function to represent the seismic performance of the substations. The fragility function for each bus is defined as the conditional probability of failure given a specific *im* value and is generally expressed as

$$P_f(im) = \Phi\left(\frac{\ln im - \lambda}{\zeta}\right) \tag{16}$$

where λ and ζ are parameters that define the shape of the fragility function that, for substations, can be derived using the state tree method proposed by Li et al. [11]. This study assumes the parameters presented in Table 1, with peak ground acceleration (PGA) selected as the IM.

To calculate the reliability index, a Monte Carlo simulation (MCS) is first conducted to estimate the likelihood of the initial disruption scenario at different *im* values. As the scale of the target system is relatively small, an assumption is made that all buses are subjected to the same *im* values. In each simulation iteration, *im* is randomly sampled, and a random number between 0 and 1 is assigned to each bus. If this random number is less than the failure probability of the corresponding bus, as determined by the fragility function, the bus is considered to have failed; otherwise, the bus is considered to have survived. Although this study does not account for the correlation between capacity and demand [38], further research is currently underway to investigate their impact on the

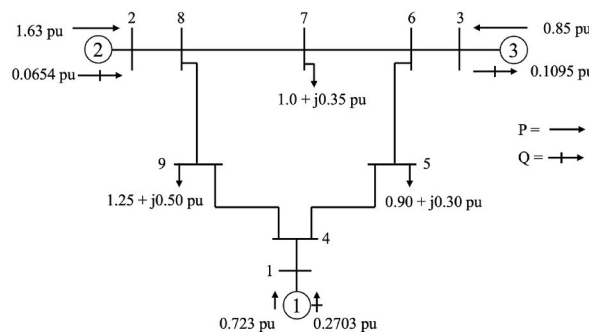


Fig. 6. IEEE 9-bus system.

Table 1
Fragility parameters.

Bus index	λ	ξ
1	0.33	0.52
2	0.52	0.43
3	0.45	0.45
4	0.70	0.58
5	0.31	0.67
6	0.49	0.22
7	0.63	0.39
8	0.58	0.40
9	0.48	0.36

resilience analysis.

A surrogate model is employed to calculate $P(F_i|im, H)$ in Eq. (4) for every im value with a small number of MCS. Among various surrogate modeling techniques, an artificial neural network (ANN) is selected for its flexibility and superior predictive performance in high-dimensional classification tasks [39]. The ANN comprises two hidden layers, each containing 256 units with a rectified linear unit activation function. The output layer utilizes a Softmax activation function to classify the 512 MECE classes (i.e., 2^9 combinations of bus failure and survival states), while the input to the neural network is a single scalar, the im value. The training dataset is generated using MCS, where the im values are uniformly divided into 42 steps ranging from 0 to 4.1g. For each step, 100 random samples were drawn, which resulted in a total of 4,200 training samples.

Note that the total computational cost to generate the training dataset, including the sequence of power flow analyses required to identify the optimal recovery sequence, takes approximately 3.6 h using an Intel i9-14900K processor. However, as the number of grid assets increases, the computational demand grows exponentially. Specifically, the number of possible recovery sequences scales factorially as $n_{fail}!$; where n_{fail} represents the number of failed components. Additionally, the number of initial disruption scenarios grows exponentially as $2^{n_{all}}$, where n_{all} denotes the total number of components in the network. These computational challenges highlight the need for efficient surrogate modeling techniques and advanced optimization strategies to enhance scalability to larger and more complex network systems.

The predicted likelihood of only the significant MECE events, as obtained through the trained ANN, is presented in Fig. 7. The significant MECE event is defined as one with a probability greater than 0.05 at least at one point along with im values. To further demonstrate the performance of the neural network in predicting the probabilities of occurrence for all MECE scenarios, their full likelihood distribution is provided in Figure A1. The significant scenarios are labeled as “CS” to denote scenarios where the buses in set S fail, while all other buses remain operational. It is observed that the scenario in which no components fail dominates at lower im values, whereas the scenario where all components fail becomes predominant as im increases. Moreover, as shown in Figure A1, the sum of $P(F_i|im, H)$ across all MECE events equals one for each im value. Alternative methods to predict $P(F_i|im, H)$ are discussed in [27].

Subsequently, the site-specific seismic characteristics are accounted for through $f_{IM}(im|H)$ in Eq. (4), which is obtained using a response spectrum from a study by Boore and Atkinson [40], following methodologies from the previous studies [27,41]. The PDF of PGA is derived under certain assumptions, including an unspecified fault type, a moment magnitude of 7, a Joyner–Boore distance of 30 km, and a shear-wave velocity of 700 m/s over the top 30 m. The estimated $f_{IM}(im|H)$ is illustrated in Figure A2 in the Appendix. However, the approach is not limited to specific hazard scenarios. Integration in Eq. (4) is performed using the trapezoidal rule.

To estimate the redundancy and recoverability indices, the blackout value is selected as the performance measure. The performance curve (i.e., Fig. 4) is, then, characterized by (1) the recovery time, (2) the shape of the recovery curve for each component, and (3) the recovery sequence; no progressive failure is assumed in this numerical investigation. In particular, a single performance is estimated for each initial disruption scenario.

First, although the recovery time for each bus would ideally be informed by comprehensive analysis and expert opinions, this study

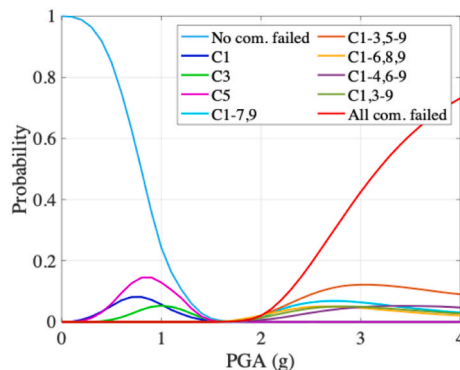


Fig. 7. Likelihood of significant initial disruption scenarios, along with im values. The “com.” in the legend represents the components.

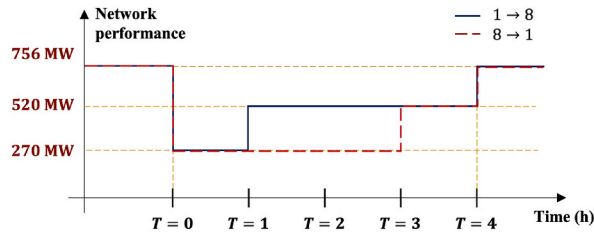


Fig. 8. Performance curves along with different recovery sequences when Nodes 1 and 8 fail.

assumes that the recovery time is proportional to the number of transmission lines connected to each bus. For instance, Bus 1, which connects only to Bus 4, has an assumed recovery time of 1 h, while Bus 8—connected to Buses 2, 7, and 9—has an assumed recovery time of 3 h. While this assumption is selected for demonstration purposes, further research is needed to refine the estimation of substation recovery times based on real-world data and operational constraints. Additionally, extending the framework to incorporate uncertainty in recovery time—such as considering probabilistic recovery sequences or random variations in restoration efforts—would enhance its realism and applicability.

Second, the performance of the power grid is considered restored once each node achieves full recovery, assuming a rectangular shape for the recovery curve. An example of this assumed recovery curve is illustrated in Fig. 8.

Third, for each initial disruption scenario, the optimal recovery sequence is adopted to minimize the area under the performance curve across all possible sequences. For instance, in a scenario where Buses 1 and 8 fail in the power grid, two possible recovery sequences exist: (1) Bus 1 followed by Bus 8 or (2) Bus 8 followed by Bus 1. The performance curves for these sequences are plotted in Fig. 8 as blue solid and red dashed lines, respectively. In this example, the sequence where Bus 1 recovers before Bus 8 is selected for calculating the redundancy and recoverability indices, as it results in the smallest area above the curve.

A β - π - γ diagram for the power network is illustrated in Fig. 9, with the resilience threshold ($RG^s / \lambda_H N_F$ in Eq. (15)) set to 0.07. A total of 13 MECE events are identified as lacking sufficient resilience, represented by red dots in the figure. From this diagram, a trend is observed that disruption scenarios with relatively high reliability (i.e., rare failure scenarios) tend to have lower redundancy and recoverability (i.e., higher initial performance loss and longer recovery times), confirming the complementary nature between indices. Moreover, Table 2 provides the number of failed scenarios in relation to varying resilience threshold values. As the resilience threshold decreases, the number of initial disruption scenarios that fail to meet the specified resilience threshold increases. Further research is needed to align resilience performance thresholds with the safety requirements outlined in design codes.

To further analyze resilience performance, a β - π - γ diagram is projected as a 2D β - π surface in Fig. 10, with colors representing recoverability index values. Fig. 10(b) presents a closer view of the red box in Fig. 10(a), using the same labeling scheme as in Fig. 7. In the figure, scenarios with blue edges represent disruption scenarios that satisfy the resilience threshold, while those with red edges indicate scenarios that do not, similar to Fig. 9. Resilience thresholds corresponding to recoverability values of $\gamma = 0.1$ and $\gamma = 0.9$ are also visualized.

The analysis yields four primary findings. First, comparing the solid lines between $\gamma = 0.1$ and $\gamma = 0.9$, as the recoverability of a scenario decreases, the corresponding resilience threshold becomes more stringent. Second, due to the extremely low probability of simultaneous failure across multiple buses, most initial disruption scenarios that fall below the resilience threshold involve up to three buses failing concurrently. Only one scenario among those involving the failure of three or more buses failed to meet the resilience threshold. Third, comparing initial disruption scenarios C3,4 and C1,3, both exhibit equivalent performance loss as Buses 1 and 4 are both connected to Generator 1, i.e., the same redundancy index. However, C1,3 meets the resilience threshold, while C3,4 does not,

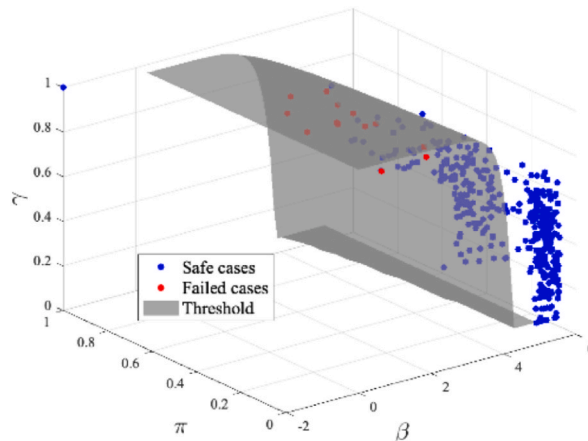


Fig. 9. Resilience performance of the power grid.

Table 2
Failed initial disruption cases, along with resilience threshold.

$RG^* / \lambda_H N_F$	Failed disruption scenarios
1	3
0.1	7
0.07	13
0.01	46
0.001	193

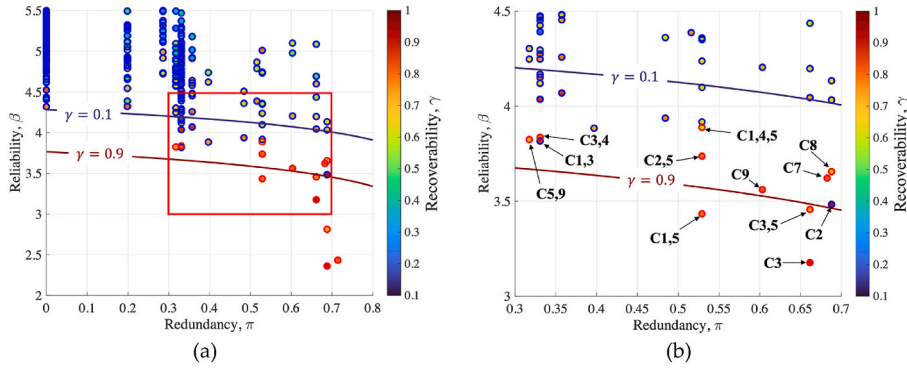


Fig. 10. β - π diagram with resilience thresholds representing different recoverability index values.

despite C3,4 having a higher reliability index ($\beta = 3.82$) than C1,3 ($\beta = 3.84$). This discrepancy arises because the recoverability index of C1,3 ($\gamma = 0.87$) is higher than that of C3,4 ($\gamma = 0.78$). Fourth, examining initial disruption scenarios C2, C7, C8, and C9, only C2 satisfies the resilience criteria, even though its reliability index is lower than those of the other scenarios. This is because C2 has higher redundancy ($\pi = 0.69$) and recoverability ($\gamma = 0.91$) indices than the others. The resilience indices and threshold values for annotated scenarios in Fig. 10(b) are detailed in Table A4 in the Appendix for further clarification. These indices and graphical tools facilitate a comprehensive understanding of the resilience performance of the network.

4.2. Transportation network with multiple bridges

This section describes the analysis of the Sioux Falls benchmark network, USA [42,43]. As shown in Fig. 11, the network comprises 76 unidirectional edges and 24 nodes. All settings are configured as described in a previous study by Lee et al. [43]. The target system performance is to ensure a timely evacuation from origin nodes n_{13} , n_{23} , and n_{24} to destination nodes n_2 , n_6 , and n_7 under an earthquake scenario. Thus, the system performance is defined as the maximum flow between the origin and destination nodes. This can be calculated by adding a virtual node n_{25} heading to the origin nodes and n_{26} headed from the destination nodes (cf. Fig. 11). The maximum flow capacities of the edges as the number of vehicles per hour are summarized in Table 3.

The network is assumed to include ten bridges, with their locations indicated in Fig. 11. These bridges are considered the only vulnerable components in the event of an earthquake. Damage probabilities are assessed following the procedure in [43], using the approximate seismic fragility from [44]. The attenuation relationship for calculating PGA and peak ground velocity from moment magnitude follows [45], consistent with [43]. Four damage states are considered: no damage (DS1), slight to moderate damage (DS2), extensive damage (DS3), and complete damage (DS4), corresponding to drift capacity levels of 2%, 4%, and predicted collapse, based on [46]. Further details on structural analysis are available in [43].

For maximum flow analysis, the damage states are assumed to correspond to 100%, 75%, 50%, and 0% of the original flow capacity, respectively. Given the relatively low seismic risk in the Sioux Falls region, the design moment magnitude is set at 5.5, with a hazard rate of $\lambda_H = 10^{-3}$. The probabilities of the damage states for each bridge are calculated using the procedure outlined in a study by Lee et al. [43]. For these calculations, bridges C3, C7, C8, and C10 are assumed to be deteriorated, while the others are considered pristine. The evaluated probabilities are summarized in Table 4. To calculate the redundancy index in Eq. (6), system performance is measured as the maximum flow between nodes n_{25} and n_{26} . Under normal conditions (i.e., all bridges in DS1), the system performance is 12,600 vehicles per hour.

For the recoverability index in Eq. (8), a recovery process is assumed, where one bridge is repaired at a time in the order of their indices (i.e., Bridge C1 \rightarrow Bridge C2 \rightarrow ... \rightarrow Bridge C10). Recovery days are based on mean values provided by FEMA [47], which are 0, 3, 73, and 250 days for DS1, DS2, DS3, and DS4, respectively. Bridges are considered closed for the entire duration of the repair. The coefficients in Eq. (10) are set as $k_R = -5.34 \cdot 10^{-4}$ and $\gamma_{\min} = 0$. The parameter values are selected such that the minimum value of $k_R T_i + 1$ becomes zero. The resilience threshold RG^* is set to 1.0.

Fig. 12 illustrates 4¹⁰ scenarios, along with the resilience threshold surface. The evaluation of the scenarios takes approximately 4.2 h using an Intel i7-1165G7 processor. Approximately 0.304% of these scenarios are classified as failed cases. Fig. 13(a) presents the

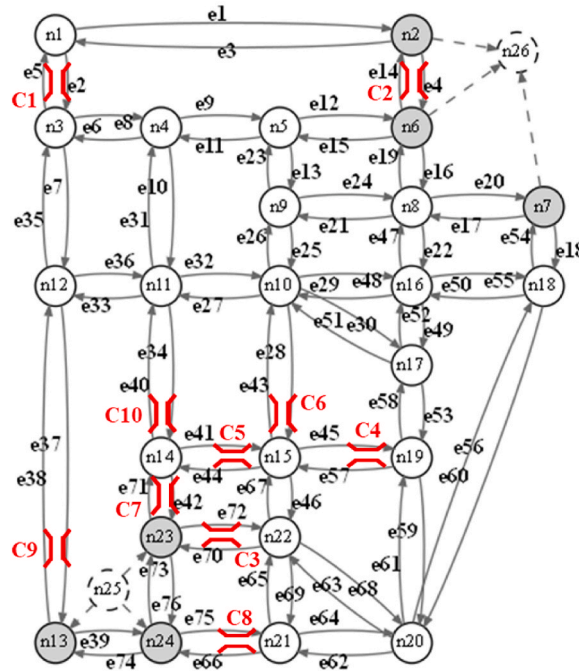


Fig. 11. Sioux Falls network with ten bridges.

Table 3

Maximum flow capacities of the edges in the Sioux Falls benchmark network (adapted from Lee et al. [43]).

Flow capacity (number of vehicles per hour)	Edge indices
1800	1, 8, 9, 16, 17, 25, 26, 32, 33, 36, 43, 50, 51, 55, 58, 68, 69, 76
3600	4, 5, 6, 7, 10, 11, 12, 13, 20, 21, 22, 23, 24, 27, 28, 29, 35, 37, 40, 41, 42, 44, 45, 46, 47, 48, 54, 56, 59, 60, 61, 62, 63, 64, 65, 66, 72, 73, 74, 75
6600	2, 3, 14, 15, 18, 19, 30, 31, 34, 38, 39, 49, 52, 53, 57, 67, 70, 71

β - π diagram, showing resilience threshold curves corresponding to recoverability indices of 0.1 and 0.9. The two threshold curves are closely spaced, with both remaining relatively flat with respect to redundancy values. This suggests that the resilience analysis in this example is most sensitive to reliability. Fig. 13(b) focuses on the range of redundancy $\pi \in [0.6, 1.0]$ and reliability $\beta \in [3.0, 8.0]$. Most of the failed cases have a recoverability index greater than 0.8, further confirming that recoverability is not the most critical factor for the system. In Fig. 13(b), four failed cases are highlighted to show the damage states of the bridges, with all these cases featuring a majority of the bridges in DS4.

The statistics for the scenarios that failed to meet the resilience requirement (red dots in Fig. 12) are analyzed in Fig. 14. Fig. 14(a) presents a box plot that shows the number of bridges in each damage state. The average number of bridges in DS4 exceeds six, indicating that the most critical scenarios are those in which a majority of the bridges are completely damaged. Fig. 14(b) displays the

Table 4

Damage probabilities of bridges in the Sioux Falls benchmark network.

	DS1	DS2	DS3	DS4
C1	$9.9699 \cdot 10^{-1}$	$2.3023 \cdot 10^{-3}$	$3.1637 \cdot 10^{-5}$	$6.7953 \cdot 10^{-4}$
C2	$9.9935 \cdot 10^{-1}$	$5.3940 \cdot 10^{-4}$	$4.6196 \cdot 10^{-6}$	$1.0552 \cdot 10^{-4}$
C3	$9.7137 \cdot 10^{-1}$	$1.9311 \cdot 10^{-2}$	$6.2287 \cdot 10^{-4}$	$8.6992 \cdot 10^{-3}$
C4	$9.9664 \cdot 10^{-1}$	$2.5518 \cdot 10^{-3}$	$3.6340 \cdot 10^{-5}$	$7.7440 \cdot 10^{-4}$
C5	$9.8680 \cdot 10^{-1}$	$9.1435 \cdot 10^{-3}$	$2.0952 \cdot 10^{-4}$	$3.8464 \cdot 10^{-3}$
C6	$9.9349 \cdot 10^{-1}$	$4.7362 \cdot 10^{-3}$	$8.4242 \cdot 10^{-5}$	$1.6915 \cdot 10^{-3}$
C7	$9.6552 \cdot 10^{-1}$	$2.2928 \cdot 10^{-2}$	$8.0000 \cdot 10^{-4}$	$1.0751 \cdot 10^{-2}$
C8	$9.6393 \cdot 10^{-1}$	$2.3902 \cdot 10^{-2}$	$8.5031 \cdot 10^{-4}$	$1.1313 \cdot 10^{-2}$
C9	$9.5129 \cdot 10^{-1}$	$3.0844 \cdot 10^{-2}$	$1.2057 \cdot 10^{-3}$	$1.6661 \cdot 10^{-2}$
C10	$9.8069 \cdot 10^{-1}$	$1.3417 \cdot 10^{-2}$	$3.6899 \cdot 10^{-4}$	$5.5254 \cdot 10^{-3}$

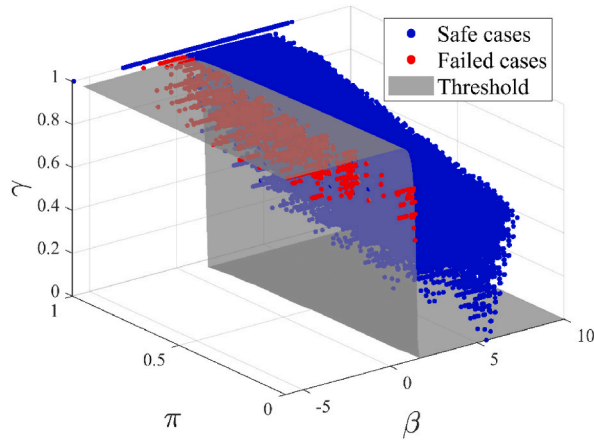


Fig. 12. Resilience performance of the Sioux Falls benchmark network.

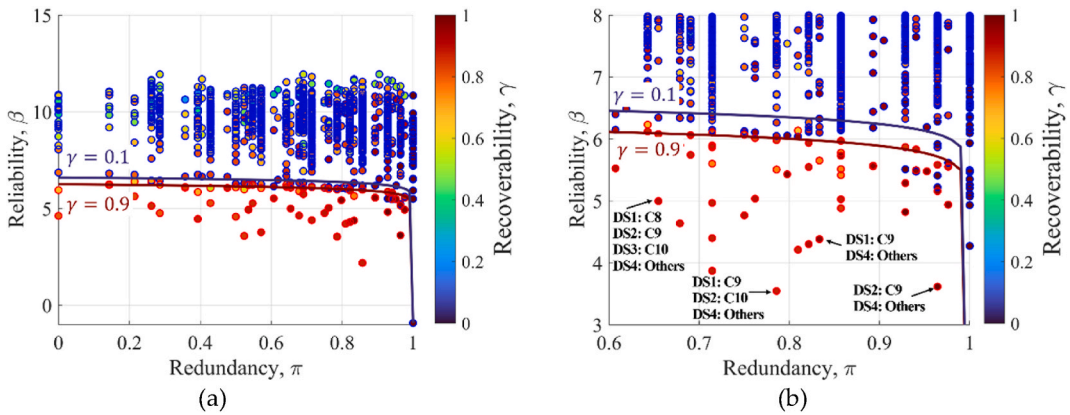


Fig. 13. β - π diagram with resilience thresholds in the Sioux Falls benchmark network: (a) over the full range of π and β and (b) focusing on the range $\pi \in [0.6, 1.0]$ and $\beta \in [3.0, 8.0]$.

occurrence of damage states DS2, DS3, and DS4 for each bridge. Bridges C2 and C4 have the highest occurrences, indicating their greater importance. As reliability is the most critical factor in this example and the damage probabilities for these two bridges are not higher than for the others, these statistics suggest that their locations are particularly critical. Although bridges C3, C7, C8, and C10 are assumed to be deteriorated, the statistics in Fig. 14(b) imply that the deterioration status does not significantly influence the resilience of the system.

5. Conclusions

This study introduced a new resilience analysis framework for lifeline networks by integrating a system-reliability-based disaster resilience analysis method with the resilience triangle model. The proposed framework defines resilience performance using three key indices: reliability, redundancy, and recoverability. These indices, estimated for each initial disruption scenario, were integrated to assess the resilience gap, identifying the most vulnerable scenarios that fail to meet the required minimum resilience. This supports decision-making for pre-hazard mitigation strategies. Additionally, the system performance curve, which describes the recovery phase through the redundancy and recoverability indices, facilitates rapid and effective decision-making in post-hazard contexts. The effectiveness and applicability of the framework were demonstrated through two numerical investigations involving power and transportation networks under seismic hazard conditions.

While the framework provides a compact and informative indication of the resilience performance of a system, applicable both before and after hazards, several aspects could be improved. First, the study assumes linear functions to convert the expected system performance loss into the redundancy index and the expected normalized recovery time into the recoverability index. However, resilience performance may vary significantly based on the choice of redundancy and recoverability indexing functions. Therefore, further research is needed to assess the sensitivity of resilience performance to different indexing functions. Second, in contrast to the *de minimis* risk framework discussed by Lim et al. [15], this study does not offer a concrete process for defining the resilience threshold, i.e., the target resilience gap RG^* in Eq. (14). As resilience quantification varies based on the specific network and the selected

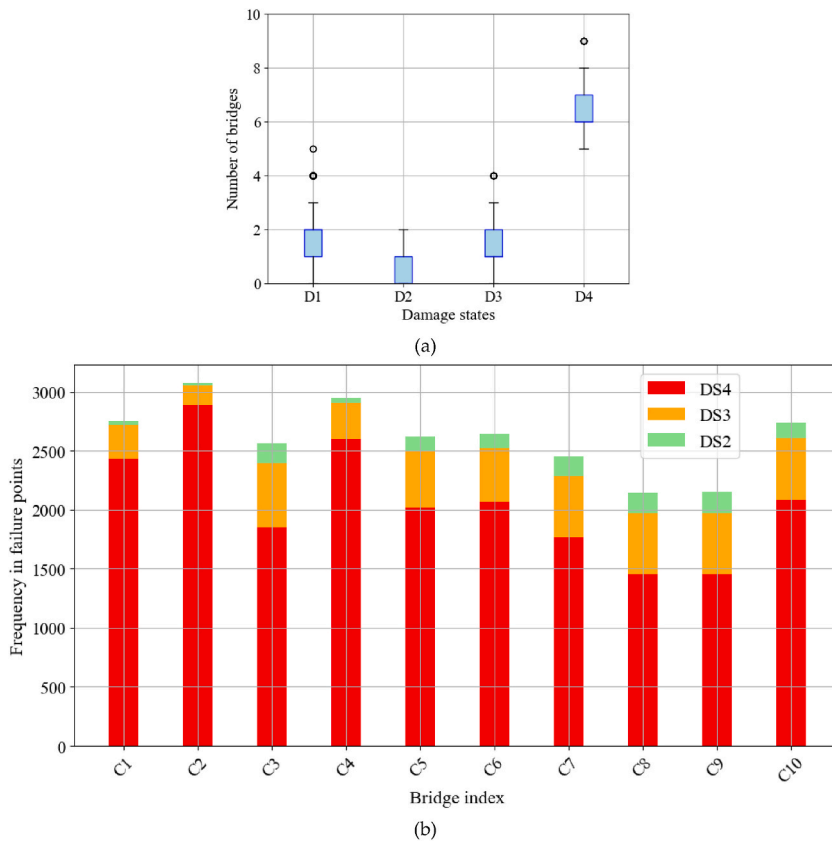


Fig. 14. Statistics of the failed cases in the Sioux Falls benchmark network: (a) box plot of the number of bridges and (b) occurrence of damage states DS2, DS3, and DS4 per bridge.

performance measures, comprehensive investigations are required to tailor the proposed concept to different lifeline networks. Third, calculating resilience indices for every initial disruption scenario incurs substantial computational costs. To address this, surrogate modeling or advanced reliability analysis techniques, such as those proposed by Kim et al. [48], should be explored. While randomness in recovery was not considered in the numerical examples, incorporating it would further increase computational costs, which remains a subject for future research. Fourth, our current framework does not explicitly consider the interaction between demand and supply of resources during the recovery phase. However, our approach can be extended by adopting the compositional demand/supply framework developed by Didier et al. [17] and Blagojević et al. [18], facilitating a more optimized post-disaster recovery process. Lastly, the need to evaluate every MECE event may limit the addressable system size. Future work can attempt to integrate advanced system reliability methods to mitigate this limitation. This study represents one of the initial efforts to quantitatively assess the resilience performance of lifeline networks. Continued refinement, particularly through the integration of advanced socio-economic analyses, will significantly enhance the practical applicability of the proposed framework.

CRedit authorship contribution statement

Taeyong Kim: Writing – original draft, Visualization, Validation, Software, Methodology, Investigation, Data curation, Conceptualization. **Sang-ri Yi:** Writing – review & editing, Validation, Supervision. **Ji Hyeon Kim:** Writing – review & editing, Validation, Supervision, Funding acquisition. **Ji-Eun Byun:** Writing – review & editing, Software, Data curation.

Declaration of competing interest

The authors declare the following financial interests/personal relationships which may be considered as potential competing interests: Taeyong Kim reports financial support was provided by Korea Railroad Research Institute. The other authors declare that they have no known competing financial interests or personal relationships that could have appeared to influence the work reported in this paper.

Acknowledgments

Funding: This work was supported by a grant from the R&D Program (Development of resilience-based prevention and recovery support technologies for railway networks under earthquake hazards, PK2402A5) of the Korea Railroad Research Institute.

Appendix A

Figure A1 presents a detailed representation of the relative frequency of all 512 MECE events as a function of PGA values. The color coding of significant scenarios in Figure A1 corresponds to those used in Fig. 7, ensuring consistency between the two visualizations.

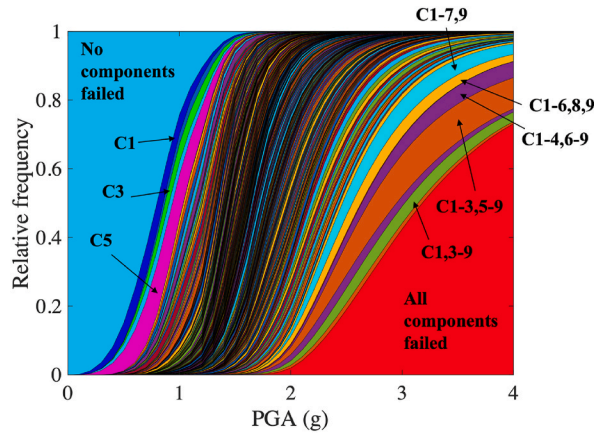


Fig. A1. Likelihood of MECE events, along with *im* values.

Figure A2 illustrates the estimated $f_{IM}(im|H)$ used to assess the resilience of the power grid system in Section 4.1.

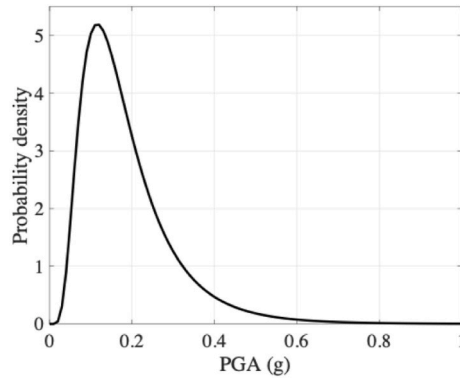


Fig. A2. PDF of *im*.

The input information of the IEEE 9 used to demonstrate the proposed resilience analysis framework is described. Generator, load, and transmission line data are given in Tables A1, A2, and A3, respectively.

Table A1

Generator data (depicted as a number within a circle in Fig. 6).

Generator	Active power	Reactive power	Maximum power
G1	72.3 MW	27.03 Mvar	250 MW
G2	163 MW	6.54 Mvar	300 MW
G3	85 MW	-10.95 Mvar	270 MW

Table A2

Load data.

Load	Active power	Reactive power
5	216 MW	72 Mvar
7	240 MW	84 Mvar
9	300 MW	120 Mvar

Table A3
Transmission line data, where node represents the bus in the grid system.

Line index	Node 1	Node 2	Maximum capacity
1	1	4	250 MW
2	4	5	250 MW
3	5	6	150 MW
4	3	6	300 MW
5	6	7	150 MW
6	7	8	250 MW
7	8	2	250 MW
8	8	9	250 MW
9	9	4	250 MW

Table A4 presents the resilience indices and threshold values corresponding to the annotated scenarios in Fig. 10(b), offering a comprehensive reference for the power network analysis discussed in Section 4.1.

Table A4
Resilience indices and threshold values for the annotated scenarios in Fig. 10(b).

Scenarios	β	π	γ	$\Phi(-\beta)f_{\pi}^{-1}(\pi)f_{\gamma}^{-1}(\gamma)$
C3	3.177	0.661	0.910	0.191
C7	3.621	0.683	0.820	0.070
C8	3.655	0.688	0.730	0.091
C9	3.561	0.603	0.820	0.111
C1,5	3.434	0.529	0.801	0.235
C2,5	3.737	0.529	0.801	0.074
C3,4	3.836	0.331	0.784	0.076
C3,5	3.456	0.661	0.758	0.189
C5,9	3.824	0.317	0.745	0.096
C1,4,5	3.888	0.529	0.581	0.084
C2	3.483	0.688	0.910	0.059
C1,3	3.817	0.301	0.868	0.050

Data availability

Data will be made available on request.

References

- [1] E.E. Koks, J. Rozenberg, C. Zorn, M. Tariverdi, M. Vousdoukas, S.A. Fraser, J.W. Hall, S. Hallegatte, A global multi-hazard risk analysis of road and railway infrastructure assets, *Nat. Commun.* 10 (2019) 2677, <https://doi.org/10.1038/s41467-019-10442-3>.
- [2] CNN Business, Saudi Oil Production Impacted by Drone Attacks, CNN, 2019. <https://edition.cnn.com/2019/09/14/business/saudi-oil-output-impacted-drone-attack/index.html>.
- [3] M. Bruneau, S.E. Chang, R.T. Eguchi, G.C. Lee, T.D. O'Rourke, A.M. Reinhorn, M. Shinozuka, K. Tierney, W.A. Wallace, D. Von Winterfeldt, A framework to quantitatively assess and enhance the seismic resilience of communities, *Earthq. Spectra* 19 (2003) 733–752, <https://doi.org/10.1193/1.1623497>.
- [4] I. Kilanitis, A. Sextos, Integrated seismic risk and resilience assessment of roadway networks in earthquake prone areas, *Bull. Earthq. Eng.* 17 (2019) 181–210, <https://doi.org/10.1007/s10518-018-0457-y>.
- [5] Y. Kwon, J. Song, System-reliability-based disaster resilience analysis of infrastructure networks and causality-based importance measure, *ASCE-ASME J. Risk Uncertain. Eng. Syst. Part B Mech. Eng.* 9 (2023), <https://doi.org/10.1115/1.4062682>.
- [6] Y. Li, Y. Dong, D.M. Frangopol, D. Gautam, Long-term resilience and loss assessment of highway bridges under multiple natural hazards, *Struct. Infrastruct. Eng.* 16 (2020) 626–641, <https://doi.org/10.1080/15732479.2019.1699936>.
- [7] S. Wang, Z. Guo, X. Huang, J. Zhang, A three-stage model of quantifying and analyzing power network resilience based on network theory, *Reliab. Eng. Syst. Saf.* 241 (2024) 109681, <https://doi.org/10.1016/j.ress.2023.109681>.
- [8] Y. Shiozaki, S. Nagamatsu, K. Sato, Y. Bhattacharya, A systematic literature review of empirical validation of disaster resilience indicators, *Int. J. Disaster Risk Reduct.* 111 (2024) 104681, <https://doi.org/10.1016/j.ijdrr.2024.104681>.
- [9] S. Farahani, A. Shojaeian, B. Behnam, M. Roohi, Probabilistic seismic multi-hazard risk and restoration modeling for resilience-informed decision making in railway networks, *Sustain. Resil. Infrastruct.* 8 (2023) 470–491, <https://doi.org/10.1080/23789689.2023.2170090>.
- [10] M. Wei, J. Xu, Assessing road network resilience in disaster areas from a complex network perspective: a real-life case study from China, *Int. J. Disaster Risk Reduct.* 100 (2024) 104167, <https://doi.org/10.1016/j.ijdrr.2023.104167>.
- [11] J. Li, T. Wang, Q. Shang, Probability-based seismic resilience assessment method for substation systems, *Struct. Infrastruct. Eng.* 18 (2022) 71–83, <https://doi.org/10.1080/15732479.2020.1835998>.
- [12] W. Sun, P. Bocchini, B.D. Davison, Resilience metrics and measurement methods for transportation infrastructure: the state of the art, *Sustain. Resil. Infrastruct.* 5 (2020) 168–199, <https://doi.org/10.1080/23789689.2018.1448663>.
- [13] A.D. González, L. Duenas-Osorio, M. Sánchez-Silva, A.L. Medaglia, The interdependent network design problem for optimal infrastructure system restoration, *Comput. Aided Civ. Infrastruct. Eng.* 31 (2016) 334–350, <https://doi.org/10.1111/mice.12171>.
- [14] B. Hou, J. Huang, H. Miao, X. Zhao, S. Wu, Seismic resilience evaluation of water distribution systems considering hydraulic and water quality performance, *Int. J. Disaster Risk Reduct.* 93 (2023) 103756, <https://doi.org/10.1016/j.ijdrr.2023.103756>.

- [15] S. Lim, T. Kim, J. Song, System-reliability-based disaster resilience analysis: framework and applications to structural systems, *Struct. Saf.* 96 (2022) 102202, <https://doi.org/10.1016/j.strusafe.2022.102202>.
- [16] M. Broccardo, P. Galanis, S. Esposito, B. Stojadinovic, Probabilistic resilience assessment of civil systems: analysis and validity of the PEER framework. *Safety and Reliability of Complex Engineered Systems, ESREL*, 2015, p. 331.
- [17] M. Didier, M. Broccardo, S. Esposito, B. Stojadinovic, A compositional demand/supply framework to quantify the resilience of civil infrastructure systems (Re-CoDeS), *Sustain. Infrastruct.* 3 (2018) 86–102, <https://doi.org/10.1080/23789689.2017.1364560>.
- [18] N. Blagojević, L. Bodenmann, Y. Reuland, B. Stojadinović, Regional recovery modeling and postdisaster model updating: the case of the 2010 Kraljevo earthquake in Serbia, *J. Struct. Eng.* 150 (2024) 05023006, <https://doi.org/10.1061/JSENDH.STENG-12334>.
- [19] ASME Innovative Technologies Institute, *All Hazards Risk and Resilience Prioritizing Critical Infrastructure Using the RAMCAP Plus Approach*, ASME Press, 2009.
- [20] M. Ouyang, L. Dueñas-Osorio, X. Min, A three-stage resilience analysis framework for urban infrastructure systems, *Struct. Saf.* 36–37 (2012) 23–31, <https://doi.org/10.1016/j.strusafe.2011.12.004>.
- [21] N. Sharma, A. Tabandeh, P. Gardoni, Regional resilience analysis: a multiscale approach to optimize the resilience of interdependent infrastructure, *Comput. Aided Civ. Infrastruct. Eng.* 35 (2020) 1315–1330, <https://doi.org/10.1111/mice.12606>.
- [22] J. Sun, K. Bathgate, Z. Zhang, Bayesian network-based resilience assessment of interdependent infrastructure systems under optimal resource allocation strategies, *Resil. Cities Struct.* 3 (2024) 46–56, <https://doi.org/10.1016/j.rcns.2024.06.001>.
- [23] Y. Xiao, X. Zhao, Y. Wu, Z. Chen, H. Gong, L. Zhu, Y. Liu, Seismic resilience assessment of urban interdependent lifeline networks, *Reliab. Eng. Syst. Saf.* 218 (2022) 108164, <https://doi.org/10.1016/j.res.2021.108164>.
- [24] R.K. Mazumder, A.M. Salman, Y. Li, Post-disaster sequential recovery planning for water distribution systems using topological and hydraulic metrics, *Struct. Infrastruct. Eng.* 18 (2022) 728–743, <https://doi.org/10.1080/15732479.2020.1864415>.
- [25] H. Liang, N. Blagojević, Q. Xie, B. Stojadinović, Seismic resilience assessment and improvement framework for electrical substations, *Earthq. Eng. Struct. Dynam.* 52 (2023) 1040–1058, <https://doi.org/10.1002/eqe.3800>.
- [26] W. Zhang, N. Wang, Resilience-based risk mitigation for road networks, *Struct. Saf.* 62 (2016) 57–65, <https://doi.org/10.1016/j.strusafe.2016.06.003>.
- [27] S.R. Yi, T. Kim, System-reliability-based disaster resilience analysis for structures considering aleatory uncertainties in external loads, *Earthq. Eng. Struct. Dynam.* 52 (2023) 4939–4963, <https://doi.org/10.1002/eqe.3991>.
- [28] M.E. Paté-Cornell, Quantitative safety goals for risk management of industrial facilities, *Struct. Saf.* 13 (1994) 145–157, [https://doi.org/10.1016/0167-4730\(94\)90023-X](https://doi.org/10.1016/0167-4730(94)90023-X).
- [29] Z. Xu, S.S. Chopra, Network-based assessment of metro infrastructure with a spatial–temporal resilience cycle framework, *Reliab. Eng. Syst. Saf.* 223 (2022) 108434, <https://doi.org/10.1016/j.res.2022.108434>.
- [30] S. Misra, J.E. Padgett, Post-Earthquake Restoration Modelling of a Railway Bridge Network, *Congress on Technical Advancement*, 2017, pp. 91–103, <https://doi.org/10.1061/9780784481028.010>.
- [31] P. Fu, X. Li, L. Xu, M. Wang, An advanced assessment framework for seismic resilience of railway continuous girder bridge with multiple spans considering 72h golden rescue requirements, *Soil Dynam. Earthq. Eng.* 177 (2024) 108370, <https://doi.org/10.1016/j.soildyn.2023.108370>.
- [32] Federal Emergency Management Agency (FEMA), *Multi-hazard Loss Estimation Methodology: Earthquake Model*, Department of Homeland Security, Washington, District of Columbia: FEMA, 2012.
- [33] F. Freddi, C. Galasso, G. Cremen, A. Dall'Asta, L. Di Sarno, A. Giaralis, F. Gutiérrez-Urzúa, C. Málaga-Chuquitaype, S.A. Mitoulis, C. Petrone, A. Sextos, L. Sousa, K. Tarbali, E. Tubaldi, J. Wardman, G. Woo, Innovations in earthquake risk reduction for resilience: recent advances and challenges, *Int. J. Disaster Risk Reduct.* 60 (2021) 102267, <https://doi.org/10.1016/j.ijdr.2021.102267>.
- [34] R. Guidotti, H. Chmielewski, V. Unnikrishnan, P. Gardoni, T. McAllister, J. van de Lindt, Modeling the resilience of critical infrastructure: the role of network dependencies, *Sustain. Resil. Infrastruct.* 1 (2016) 153–168, <https://doi.org/10.1080/23789689.2016.1254999>.
- [35] L. Dueñas-Osorio, J.I. Craig, B.J. Goodno, Seismic response of critical interdependent networks, *Earthq. Eng. Struct. Dynam.* 36 (2007) 285–306, <https://doi.org/10.1002/eqe.626>.
- [36] M.C. Shekar, N. Aarthi, Contingency analysis of IEEE 9 bus system, in: *3rd IEEE International Conference on Recent Trends in Electronics, Information & Communication Technology (RTEICT)*, IEEE, 2018, pp. 2225–2229, <https://doi.org/10.1109/RTEICT42901.2018.9012467>.
- [37] P.M. Anderson, A.A. Fouad, *Power System Control and Stability*, John Wiley & Sons, 2008.
- [38] C. Kang, T. Kim, O.S. Kwon, J. Song, Deep neural network-based regional seismic loss assessment considering correlation between EDP residuals of building structures, *Earthq. Eng. Struct. Dynam.* 52 (2023) 3414–3434, <https://doi.org/10.1002/eqe.3775>.
- [39] T. Kim, O.S. Kwon, J. Song, Response prediction of nonlinear hysteretic systems by deep neural networks, *Neural Netw.* 111 (2019) 1–10, <https://doi.org/10.1016/j.neunet.2018.12.005>.
- [40] D.M. Boore, G.M. Atkinson, Ground-motion prediction equations for the average horizontal component of PGA, PGV, and 5%-damped PSA at spectral periods between 0.01 s and 10.0 s, *Earthq. Spectra* 24 (2008) 99–138, <https://doi.org/10.1193/1.2830434>.
- [41] T. Kim, S.R. Yi, Accelerated system-reliability-based disaster resilience analysis for structural systems, *Struct. Saf.* 109 (2024) 102479, <https://doi.org/10.1016/j.strusafe.2024.102479>.
- [42] S. Ukkusuri, *Accounting for Uncertainty, Robustness and Online Information in Transportation Networks*. Thesis (PhD), University of Texas at Austin, 2005.
- [43] Y.J. Lee, J. Song, P. Gardoni, H.W. Lim, Post-hazard flow capacity of bridge transportation network considering structural deterioration of bridges, *Struct. Infrastruct. Eng.* 7 (2011) 509–521, <https://doi.org/10.1080/15732479.2010.493338>.
- [44] Q. Huang, P. Gardoni, S. Hurlbaas, Probabilistic seismic demand models and fragility estimates for reinforced concrete highway bridges with one single-column bent, *J. Eng. Mech.* 136 (2010) 1340–1353, [https://doi.org/10.1061/\(ASCE\)EM.1943-7889.0000186](https://doi.org/10.1061/(ASCE)EM.1943-7889.0000186).
- [45] K.W. Campbell, Empirical near-source attenuation relationships for horizontal and vertical components of peak ground acceleration, peak ground velocity, and pseudo-absolute acceleration response spectra, *Seismol. Res. Lett.* 68 (1997) 154–179, <https://doi.org/10.1785/gssrl.68.1.154>.
- [46] D.E. Choe, P. Gardoni, D. Rosowsky, Closed-form fragility estimates, parameter sensitivity, and Bayesian updating for RC columns, *J. Eng. Mech.* 133 (2007) 833–843, [https://doi.org/10.1061/\(ASCE\)0733-9399\(2007\)133:7\(833\)](https://doi.org/10.1061/(ASCE)0733-9399(2007)133:7(833)).
- [47] Federal Emergency Management Agency (FEMA), *HAZUS-MH Earthquake Model Technical Manual*, Federal Emergency Management Agency, Washington, District of Columbia, 2024.
- [48] J. Kim, S.R. Yi, J. Park, T. Kim, Efficient system reliability-based disaster resilience analysis of structures using importance sampling, *J. Eng. Mech.* 150 (2024) 04024081, <https://doi.org/10.1061/JENMDT.EMENG-7800>.